Atherosclerosis 398 (2024) 118622

Contents lists available at ScienceDirect

Atherosclerosis

journal homepage: www.elsevier.com/locate/atherosclerosis

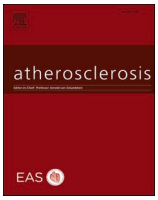

Shear stress is uncoupled from atheroprotective KLK10 in atherosclerotic plaques

Ziqi Zhou [a,1], Suze-Anne Korteland [b,1], Blanca Tardajos-Ayllon [d,a], Junxi Wu [c], Emily Chambers [a], Julia Weninck [b], Michael Simons [e], Mark Dunning [f], Torsten Schenkel [g], Mannekomba Diagbouga [d,a], Jolanda Wentzel [b], Maria Fragiadaki [d], Paul C. Evans [d,a,*]

[a] Department of Infection, Immunity and Cardiovascular Disease, INSIGNEO Institute, and the Bateson Centre, University of Sheffield, Sheffield, UK
[b] Department of Cardiology, Erasmus Medical Center, University Medical Center Rotterdam, 3015 GD, Rotterdam, the Netherlands
[c] Department of Biomedical Engineering, University of Strathclyde, Glasgow, G1 1QE, UK
[d] Centre for Biochemical Pharmacology, William Harvey Research Institute, Barts and the London School of Medicine and Dentistry, Queen Mary University of London, London, UK
[e] Department of Internal Medicine, Yale Cardiovascular Research Center, New Haven, CT, United States
[f] Sheffield Bioinformatics Core, The Medical School, University of Sheffield, Sheffield, UK
[g] Department of Engineering and Mathematics, Sheffield Hallam University, Sheffield, UK

A B S T R A C T

Background and aims: Physiological shear stress promotes vascular homeostasis by inducing protective molecules in endothelial cells (EC). However, physiological shear stress has been linked to atherosclerosis progression in some individuals with heightened cardiovascular risk. To address this apparent paradox, we hypothesized that diseased arteries may exhibit reduced responsiveness to the protective effects of physiological shear stress. Consequently, we compared the transcriptome of EC exposed to physiological shear stress in healthy arteries *versus* atherosclerotic conditions.
Methods: Employing 3D light sheet imaging and computational fluid dynamics, we identified NOS3 as a marker of physiological shear stress in both healthy and atherosclerotic murine arteries. Single-cell RNA sequencing was performed on EC from healthy (C57BL/6) mice, mildly diseased ($Apoe^{-/-}$ normal diet) mice, and highly diseased ($Apoe^{-/-}$ high fat diet) mice. The transcriptomes of $Nos3^{high}$ cells (exposed to physiological shear stress) were compared among the groups.
Results: $Nos3^{high}$ EC were associated with several markers of physiological shear stress in healthy arteries. Clustering of $Nos3^{high}$ EC revealed 8 different EC subsets that varied in proportion between healthy and diseased arteries. Cluster-specific nested functional enrichment of gene ontology terms revealed that $Nos3^{high}$ EC in diseased arteries were enriched for inflammatory and apoptotic gene expression. These alterations were accompanied by changes in several mechanoreceptors, including the atheroprotective factor KLK10, which was enriched in $Nos3^{high}$ EC in healthy arteries but markedly reduced in severely diseased arteries.
Conclusions: Physiological shear stress is uncoupled from atheroprotective KLK10 within atherosclerotic plaques. This sheds light on the complex interplay between shear stress, endothelial function, and the progression of atherosclerosis in individuals at risk of cardiovascular complications.

1. Introduction

Atherosclerosis, a lipid-driven disease characterized by arterial wall lesions containing lipids, immune cells, and other materials, is influenced by mechanical wall shear stress generated by flowing blood [1–4]. Preclinical studies and histological analyses of human arteries reveal that physiological high shear stress (HSS) prevents the initiation of atherosclerosis [5–8]. However, controversy remains regarding the influence of shear stress on the progression of atherosclerosis towards rupture-prone plaques [9,10]. Studies utilizing biplane coronary angiography, coronary intravascular ultrasound, and computational fluid dynamics have reconstructed three-dimensional (3D) arteries, revealing that physiological HSS predicts reduced plaque area and lumen patency in patients with acute coronary syndrome [11–13]. Conversely, analysis of plaque composition using virtual histology IVUS and computational fluid dynamics suggests that physiological or supraphysiological HSS is indicative of plaque instability in individuals with stable angina [14]. These discrepant findings are challenging to reconcile and may stem, in part, from differences in technologies and patient demographics [9]. A possible explanation that we examine here

* Corresponding author. Vascular Metabolism, Centre for Biochemical Pharmacology, William Harvey Research Institute, Barts and the London School of Medicine and Dentistry, Queen Mary University of London, London, UK,
E-mail address: paul.evans@qmul.ac.uk (P.C. Evans).
[1] These authors contributed equally to this work.

https://doi.org/10.1016/j.atherosclerosis.2024.118622
Received 30 June 2023; Received in revised form 2 October 2024; Accepted 3 October 2024
Available online 4 October 2024
0021-9150/© 2024 The Authors. Published by Elsevier B.V. This is an open access article under the CC BY license (http://creativecommons.org/licenses/by/4.0/).

is that the effects of HSS on vascular biology differ between health and disease.

In healthy arteries, physiological HSS is associated with vascular protection, as it elicits significant effects on the endothelium by inducing the expression of protective transcripts [15]. Since some clinical studies suggest that physiological or supra-physiological HSS within plaques may instead correlate with pathological changes, we hypothesized that the transcriptome of EC experiencing HSS might differ between healthy arteries and plaques. Our study aims to elucidate this difference by comparing the transcriptomes of cells exposed to HSS in healthy arteries *versus* plaques. To address this, we first established that endothelial nitric oxide synthase 3 (NOS3; eNOS) is a marker of HSS in atherosclerotic plaques as well as healthy arteries. Leveraging this discovery, we proceeded to compare the transcriptomic profiles of $Nos3^{high}$ cells (indicative of HSS) in healthy arteries and plaques. Using single-cell RNA sequencing (scRNAseq) of EC obtained from murine aortas categorized as healthy, mildly diseased (*Apoe*$^{-/-}$ normal diet; ND), or highly diseased (*Apoe*$^{-/-}$ high fat diet; HFD), we compared the transcriptomes of $Nos3^{high}$ cells across these groups. Our analysis revealed substantial variation in the transcriptome of $Nos3^{high}$ cells between healthy arteries, mildly diseased arteries, and severely diseased arteries, suggesting that disease modifies the endothelial transcriptome under conditions of physiological HSS. This observation potentially elucidates why HSS fails to confer protection in plaques in some groups of patients.

2. Materials and methods

2.1. Mice

C57BL/6 mice were purchased from Charles River. C57BL/6 *Apoe*$^{-/-}$ mice (JAX SN:002052) mice were fed a Western diet (40 % kcal% fat, 1.25 % cholesterol, 0 % cholic acid) for 4 or 16 weeks (Research Diets), starting at the age of 8 weeks. C57BL/6 and *Apoe*$^{-/-}$ mice were housed under specific-pathogen free conditions. Animal care and experimental procedures were performed under the UK Animal (Scientific Procedures) Act 1986 under licenses issued by the UK Home Office and local ethical committee approval was obtained. Experiments involving *Apoe*$^{-/-}$ mice were reviewed and approved by the Yale University Institutional Animal Care and Use Committee.

2.2. En face immunofluorescent staining and confocal microscopy

The expression levels of NOS3 were assessed in EC at regions of the inner curvature and outer curvature of murine aortas by *en face* staining [16] using specific primary antibodies (D9A5L; Cell Signaling Technology). EC were identified by co-staining using anti-CDH5 (BD Pharmingen) or anti-CD31 (Dianova) antibodies. Nuclei were identified using DAPI. Stained vessels were mounted prior to visualization of endothelial surfaces *en face* using confocal microscopy (Olympus SZ1000 confocal inverted microscope). The expression of specific proteins at each site was assessed by quantification of the mean fluorescence intensities with standard error of the mean.

2.3. Immunofluorescent staining of cleared tissues and light-sheet microscopy

Aortas were cleared using a CUBIC protocol adapted from Ref. [17]. Aortic arches were incubated in 50 % CUBIC-1 solution (25 % urea; 25 % Quadrol; 15 % Triton X-100) at room temperature for 2–3 h, and then in 100 % CUBIC-1 at room temperature overnight. After washing in PBS, tissues were incubated with 50 % CUBIC-2 (25 % urea, 50 % sucrose, 10 % triethanolamine) at room temperature for 1 h, and then with 100 % CUBIC-2 at room temperature overnight. After optical clearing, immunofluorescent staining was performed as above and then mounted using 2 % agarose gel in a glass capillary and imaged by light-sheet microscopy (Zeiss Light-sheet Z.1). Imaris (9.0.1) software was used to view the images and calculate fluorescence intensities.

2.4. Optical Projection Tomography (OPT) imaging and computational fluid dynamics

Fixed artery samples were processed for OPT as previously described [18]. Briefly, each sample was embedded in filtered 1.5 % low-melting-point agarose, dehydrated in absolute methanol (twice, 24 h each) and then optically cleared in 1:2 v/v benzyl alcohol: benzyl benzoate (BABB) for 24 h. Arteries were imaged using a Bioptonics 3001 OPT tomograph (SkyScan, UK). The GFP1 channel was used to capture the autofluorescence from vascular soft tissue (mainly collagen and elastin). Projection images (× 400) were obtained with a 0.9° rotation step, and these were reconstructed into a 3-dimensional image that contained a stack of 1024 cross-sections using NRecon software (Skyscan) with a resolution of 8 × 8 × 8 μm/voxels. The lumen of the artery was segmented on the green channel/cam1_T2 channel in 3D slicer (3D Slicer, version 4.4.0 [19]) using level tracing with manual adjustment. The segmentation was then smoothed to remove segmentation artefacts using a Gaussian filter. Flow extensions were added to the geometry using VMTK (Vascular Modelling Toolkit, www.vmtk.org [20]) with the inlet extended 4 times the radius to ensure a smooth inlet profile. Outlets were extended 3 times the radius to exclude upstream effects of the imposed boundary conditions. Then the geometry was imported into ANSYS ICEM (ANSYS 2021 R1) to generate a mesh. The typical cell size of healthy aortas was 0.05 mm, resulting in a mesh with 477858 elements/142384 nodes. The typical cell size of aortas that included plaques was 0.05 mm, resulting in a mesh with 584199 elements/188061 nodes. After meshing, computational fluid dynamic simulation was performed. The flow was modelled as laminar and stationary with an inlet average velocity of 0.26 m/s resulting in a typical flow for mouse aorta, for the outlet a flow split of 70 %, 16 %, 8 % and 6 % was assumed for descending aorta, brachiocephalic artery, left common carotid artery and subclavian artery, respectively [21].

2.5. NOS3 expression quantification

To obtain local NOS3 expression, the local intensity of the red channel was extracted in a region close to the lumen. Therefore, the lumen segmentation was used and vectors normal to the lumen surface were computed. These surface normals were then used to construct profiles of the NOS3 intensity across the wall perpendicular to the lumen surface. Using an intensity threshold on the green channel of 350 (healthy) or 255 (plaque) to exclude background signal, only parts of the profile above the threshold were taken into account to compute the representative NOS3 value on the red channel. The representative NOS3 intensity value was then computed as the mean intensity of the pixels along 150 μm of the normal profile across the wall.

2.6. Correlation of shear stress with NOS3 fluorescence

2D shear stress and NOS3 maps were generated by computing the centreline of the 3D geometry and using this centreline information to compute the abscissa metric (distance along the centreline) and angular metric (angle in circumference) with vmtk (Vascular Modelling Toolkit, www.vmtk.org). These two variables were used to open the 3D geometry along the longitudinal axis into a 2D map. To reduce the effect of local variation in shear stress and NOS3 intensity the 2D maps were patched into larger regions of 0.1 mm longitudinally and 22.5° circumferentially and an average value of the quantity of interest was computed for each region.

2.7. scRNAseq

Aortic ECs were enzymatically digested to generate a single cell suspension and $CD31^{+}$ $CD45^{-}$ $TOPRO3^{-}$ cells were sorted prior to

scRNAseq as reported [22,23]. Single cell counts matrix data generated from healthy mice and *ApoE*$^{-/-}$ mice exposed to ND or HFD (N = 2 pooled per group) were analysed using R (version 4.1) and Seurat (v3.2.2). For quality control purposes, data were filtered to remove cells that had less than 1500 genes or less than 3000 unique molecules identified (UMIs). Cells with more than 5 % mitochondrial genes per cell were also eliminated. For the healthy group, 684 EC were captured and 545 cells passed quality control and were analysed. For the *ApoE*−/− ND group, 1103 EC were captured and 851 analysed. For the *ApoE*−/− HFD group, 974 EC were captured and 762 analysed. Data from *ApoE*$^{-/-}$ ND, *ApoE*$^{-/-}$ HFD and healthy mice were log normalised. They were then integrated within Seurat to identify or 'anchor' cell populations that are present across the different datasets to minimise batch differences. Dimensional reduction of the data was carried out using PCA and UMAP and then clustering of the cells was calculated by working out distance metrics of nearest neighbours using the Louvain algorithm. The merged data was analysed using BBrowser 2.10.10. Gene ontology analysis was carried out using the DAVID and Metascape databases and putative mechanoreceptors were identified by literature searches based on their intracellular localization at the cell surface and function in other settings.

2.8. Statistical analysis

All statistical analysis was performed in Graph Pad Prism 8 Software. The statistical test used for each data set is stated in the figure legends. p value < 0.05 was considered to be significant.

3. Results

3.1. NOS3 is a marker of physiological HSS in healthy arteries and plaques

We sought a marker that can identify EC exposed to physiological HSS in healthy and atherosclerotic arteries. NOS3 (eNOS) was investigated since it is an established shear stress-responsive molecule [24,25]. Initially, NOS3 immunofluorescent staining was validated by analysis of aortas from healthy mice. Computational fluid dynamics previously revealed that the outer curvature of the murine aorta is exposed to higher shear stress compared to the inner [21,26]. *En face* staining coupled to confocal laser-scanning microscopy revealed that the anti-NOS3 fluorescent signal was significantly higher at the outer curvature compared to the inner curvature (Fig. 1), indicating enrichment of NOS3 under HSS conditions. To further validate this observation, we analysed whether NOS3 expression correlated with the HSS markers KLF2 and KLK10. Co-staining revealed enrichment of NOS3-positive/KLK10-positive (Supplementary Fig. S1A) and NOS3-positive/KLF2-positive (Supplementary Fig. S1B) endothelial cells at the HSS region. We conclude that NOS3 immunofluorescent staining of EC correlates with physiological HSS in healthy aortas.

To compare the spatial distribution of NOS3 and shear stress in atherosclerotic plaques, we developed a novel methodology that couples light-sheet imaging with shear stress mapping in complex geometries. To validate this approach, we initially analysed aortic arches from healthy mice. They were optically cleared (Fig. 2A) prior to immunofluorescent staining using anti-NOS3 antibodies. 3D light-sheet imaging showed that NOS3 immunofluorescence was higher in the outer

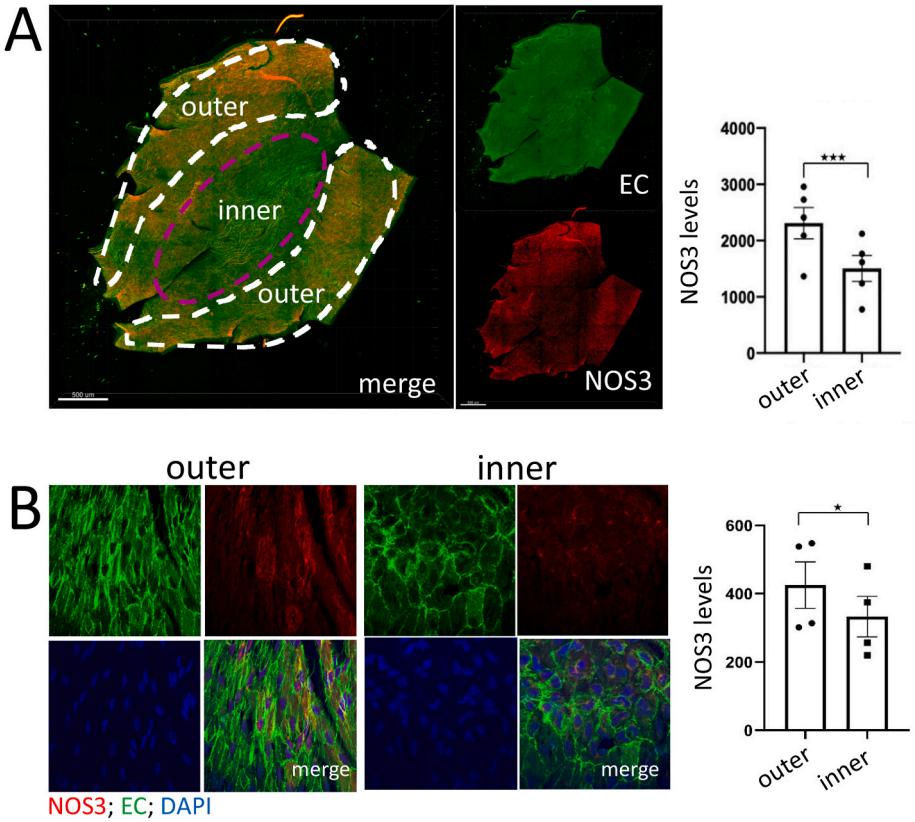

Fig. 1. *En face* staining shows enrichment of NOS3 at the outer curvature of the healthy murine aorta.
Aortic arches were isolated from healthy C57BL/6 mice aged 6–8 weeks and *en face* immunostaining was performed using anti-NOS3 antibodies (red). Endothelial cells were co-stained (EC; CD31; green) and nuclei detected using DAPI (blue). Fluorescence was analysed by laser scanning confocal microscopy. (A) Tiled images are shown with inner and outer portions of the aortic arch indicated. (B) Representative single fields of view are shown from outer and inner regions of the aortic arch. Fluorescence was quantified at outer and inner portions. Each data point represents an animal. Differences between means were analysed using a *t*-test. (For interpretation of the references to colour in this figure legend, the reader is referred to the Web version of this article.)

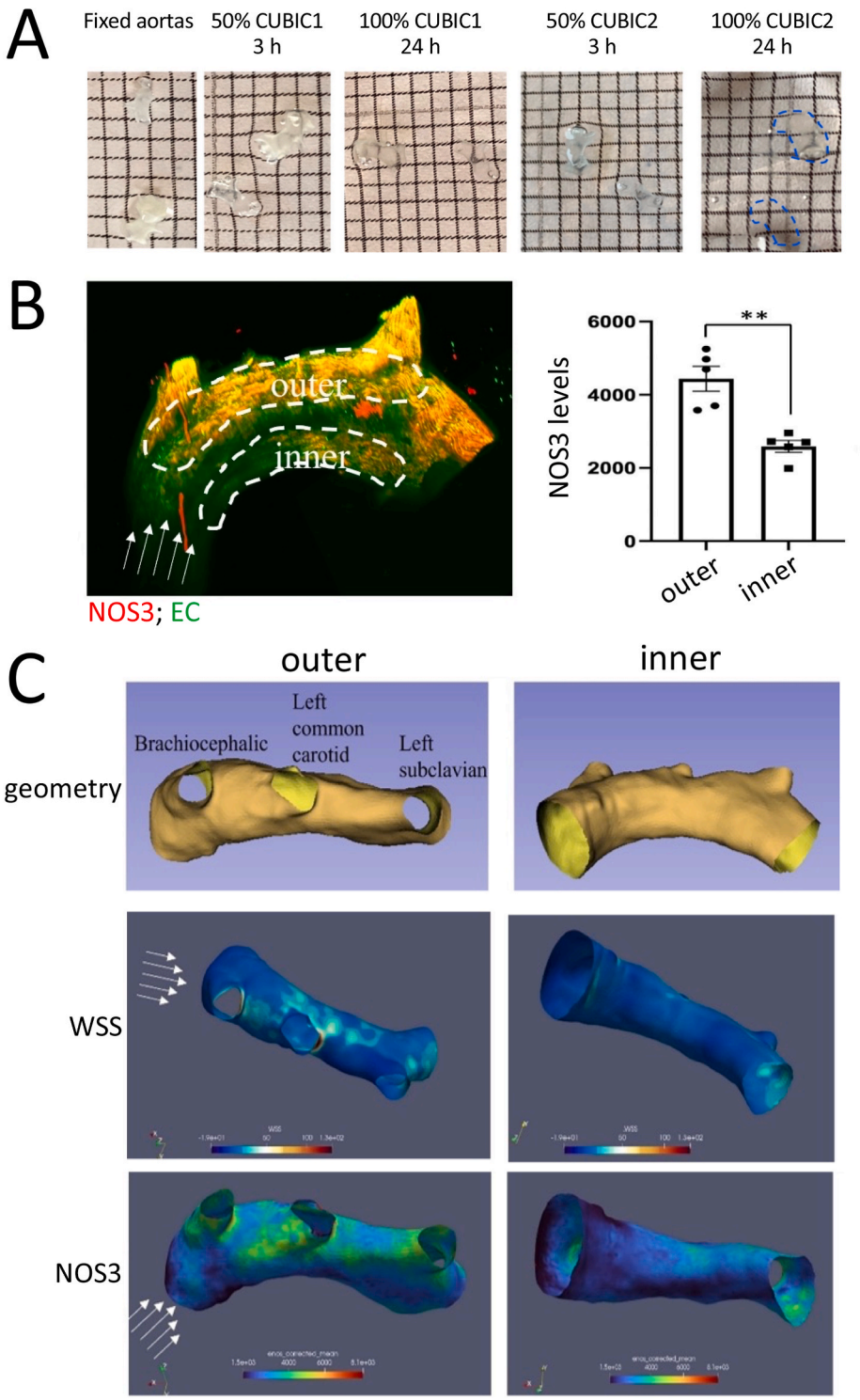

Fig. 2. 3D light-sheet imaging to compare NOS3 expression and shear stress in the healthy murine aorta.
Aortic arches were isolated from healthy C57BL/6 mice aged 6–8 weeks after perfusion fixation. Arches were optically cleared by immersion in CUBIC1 and CUBIC2. (A) Representative images are shown at several stages of the optical clearance process. (B, C) Optically-cleared aortic arches were immunostained using anti-NOS3 antibodies (red) and endothelial cells were co-stained (EC; CDH5; green) prior to analysis by light-sheet microscopy. (B) A representative image is shown. Fluorescence was quantified at outer and inner portions. Each data point represents an animal. Differences between means were analysed using a *t*-test. (C) Optically-cleared aortic arches were imaged by OPT and reconstructed geometries were used for computational fluid dynamic modelling. A representative geometry is shown alongside corresponding spatial maps of time-averaged shear stress and NOS3. (For interpretation of the references to colour in this figure legend, the reader is referred to the Web version of this article.)

curvature compared to inner curvature (Fig. 2B), which is consistent with conventional *en face* staining (Fig. 1). To analyze the spatial relationship between shear stress and NOS3 in more detail, we generated case-specific shear stress maps of the aorta. Shear stress was mapped onto aorta geometries that were reconstructed using OPT images segmented automatically with manual adjustment. High quality meshes were created and used for steady state computational fluid dynamics. Shear stress was elevated in the outer curvature compared to the inner curvature (Fig. 2C). Shear stress maps were co-registered with NOS3 distributions so that shear stress could be correlated spatially with NOS3 at multiple points. Visual inspection suggested that NOS3 values were elevated at regions of HSS e.g. outer curvature (Fig. 2C, Supplementary movie 1). This was analysed quantitatively by generating 2D maps of NOS3 and shear stress (unfolding over a longitudinal axis) (Fig. 3A–B, Fig. 3C). Averaging of values along longitudinal axes revealed that shear stress correlated positively with the NOS3 signal (Fig. 3D). We conclude that our workflow using light sheet microscopy coupled to computational fluid dynamics is able to capture and quantify the spatial relationship between shear stress and NOS3 in healthy murine aortas.

Supplementary video related to this article can be found at doi:10.1016/j.atherosclerosis.2024.118622

We next used this workflow to investigate the relationship between NOS3 and shear stress in plaques using aortic arches from *ApoE*$^{-/-}$ mice exposed to a HFD for 16 weeks. Control antibodies produced minimal fluorescence, indicating that non-specific binding of IgG to plaque is low (Supplementary Fig. S2). 3D light-sheet imaging of anti-NOS3 staining revealed a high signal at the outer curvature and at the plaque. Notably, NOS3 was elevated at the proximal part of the plaque, a potential HSS region, compared to the distal part (Fig. 4A and B, Supplementary movie 2). Consistently, 2D maps and quantitative analysis revealed a positive correlation between shear stress and NOS3 expression (Fig. 4C–E). Thus, NOS3 is a marker of physiological HSS in murine plaque endothelium. Collectively, these observations suggest that NOS3 can be used to identify EC under HSS conditions in plaques and healthy arteries.

Supplementary video related to this article can be found at doi:10.1016/j.atherosclerosis.2024.118622

3.2. *Single cell sequencing captures Nos3*^{high} *cells with HSS transcriptional signatures*

The transcriptome of HSS endothelium was compared in healthy and atherosclerotic murine arteries by performing scRNAseq. CD31^{+} CD45^{-} aortic EC were isolated from aortas of three groups of mice: healthy, mildly diseased (*Apoe*$^{-/-}$ ND) or highly diseased (*Apoe*$^{-/-}$ HFD). scRNAseq revealed 10 distinct clusters of cells (Supplementary Fig. S3A). Of these, six distinct clusters (0, 1, 2, 3, 5, 8) expressed canonical endothelial cell markers (*Pecam1*, *Cdh5* and *Vwf*; Supplementary Fig. S3B) whereas cluster 7 was enriched for genes that regulate lipid transport and cluster 9 was enriched for lymphatic endothelial markers. By contrast, cells in clusters 4 and 6 expressed smooth muscle cell (SMC)

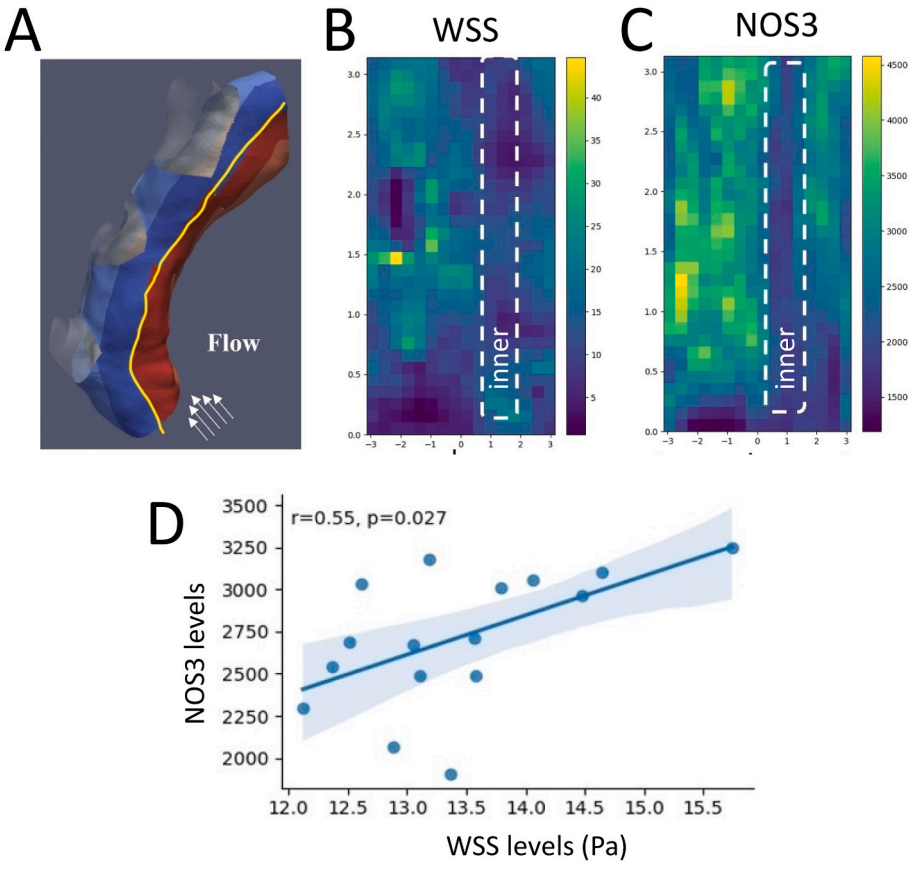

Fig. 3. NOS3 correlates with shear stress in the healthy murine aorta.
Aortic arches were isolated from healthy C57BL/6 mice aged 6–8 weeks after perfusion fixation. Arches were optically cleared by immersion in CUBIC1 and CUBIC2. Optically-cleared aortic arches were immunostained using anti-NOS3 antibodies and analysed by light-sheet microscopy. They were subsequently imaged by OPT and reconstructed 3D geometries were used for computational fluid dynamic modelling and mapping of time-averaged shear stress. (A) A representative 3D geometry is shown. Outer (blue) and inner (red) surfaces are indicated and their interface shown (yellow line). (B) A 3D map of time-averaged shear stress was flattened to form a 2D version. The inner portion is indicated (white broken line). (C) A 3D map of NOS3 was flattened to form a 2D version. The inner portion is indicated (white broken line). (D) shear stress and NOS3 levels were averaged along 16 portions of the longitudinal axis and values are plotted. A regression analysis was performed and the line of best fit is shown. (For interpretation of the references to colour in this figure legend, the reader is referred to the Web version of this article.)

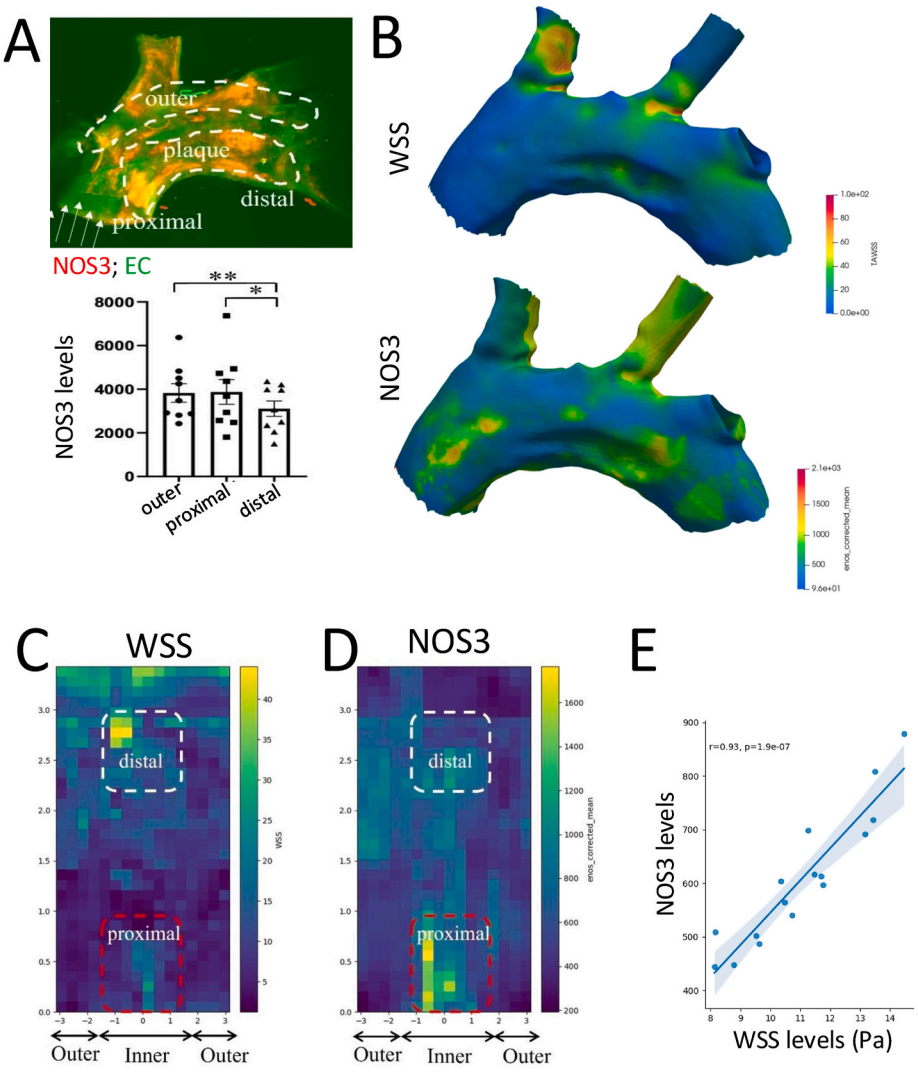

Fig. 4. NOS3 correlates with shear stress in the atherosclerotic murine aorta.
Aortic arches were isolated from *ApoE*$^{-/-}$ mice aged 6–8 weeks that were exposed to high fat diet for 12 weeks. Arches were optically cleared by immersion in CUBIC1 and CUBIC2 and then immunostained using anti-NOS3 antibodies (red). Endothelial cells were co-stained (EC; CDH5; green) prior to analysis by light-sheet microscopy. (A) A representative image is shown. Fluorescence was quantified at the outer portion and at regions positioned upstream (proximal) or downstream (distal) from the plaque. Each data point represents an animal. Differences between means were analysed using a one-way ANOVA. (B) Reconstructed geometries were used for computational fluid dynamic modelling and time-averaged shear stress (upper) and NOS3 (lower) were mapped over the surface. (C) A 3D map of time-averaged shear stress was flattened to form a 2D version. The outer and inner portions are indicated. The regions positioned distal (white broken line) or proximal (red broken line) to the plaque are indicated. (D) A 3D map of NOS3 was flattened to form a 2D version. The outer and inner portions are indicated. The regions positioned distal (white broken line) or proximal (red broken line) to the plaque are indicated. (E) shear stress and NOS3 levels were averaged along 16 portions of the longitudinal axis and values are plotted. A regression analysis was performed and the line of best fit is shown. (For interpretation of the references to colour in this figure legend, the reader is referred to the Web version of this article.)

or fibroblast markers (*Myh11, Myl9, Tagln*; Supplementary Fig. S3B). To allow comparison with other scRNAseq analysis of murine aortas we mapped the expression of signature genes from published clusters [27–29] onto the clusters that we identified (Supplementary Fig. S4, Supplementary Fig. S5, Supplementary Fig. S6). For example, EC1 from Kalluri et al. [27] has similarity to canonical ECs (clusters 0,1, 2, 3, 5, 8), EC2 resembles lipid transport cluster 7 from our analysis, and EC3 resembles cluster 9 (Supplementary Fig. S4).

EC expressing high levels of *Nos3* (*Nos3*^{high}) were selected after setting a threshold level (Supplementary Fig. S7). In healthy arteries, several HSS markers (*Klk10, Klf2, Klf4*) were expressed in a higher proportion of cells in the *Nos3*^{high} population compared to the *Nos3*^{low} population (Supplementary Fig. S8; Table S1). *Klk10, Klf2 and Klf4* were also enriched in the *Nos3*^{high} population compared to the *Nos3*^{low} population of highly diseased arteries (*ApoE*$^{-/-}$ HFD), albeit to a lesser extent than healthy arteries (Supplementary Fig. S8; Table S1). In healthy arteries, several LSS markers (*Bmp4, Lmo4, Icam1*) were expressed in a higher proportion of cells in the *Nos3*^{low} population compared to the *Nos3*^{high} population (Supplementary Fig. S9; Table S2). Collectively, these data validate the selection of the *Nos3*^{high} population to represent cells exposed to HSS.

3.3. Shear stress-regulated transcriptome differs between healthy and atherosclerotic arteries

The transcriptional signatures of *Nos3*^{high} and *Nos3*^{low} EC were compared for healthy, mildly diseased (*Apoe*$^{-/-}$ ND) and highly diseased (*Apoe*$^{-/-}$ HFD) mice. UMAP analysis revealed that *Nos3*^{high} and *Nos3*^{low} EC from healthy and diseased aortas exhibit different clustering patterns suggesting that they are associated with different

transcriptional profiles (Fig. 5A). This was investigated in greater detail by mapping *Nos3*^{high} and *Nos3*^{low} EC from healthy and diseased aortas onto specific EC clusters (compare Fig. 5A with Fig. 5B). Focusing on EC exposed to HSS, it was observed that *Nos3*^{high} EC from *ApoE*$^{-/-}$ HFD highly diseased aortas exhibited a striking increase in cluster 1 and a reduction in clusters 2 and 8 compared to *Nos3*^{high} EC from healthy aortas (Fig. 5C). Gene ontology analysis of EC clusters revealed that several terms associated with atherosclerosis ("inflammatory response", "regulation of leukocyte cell-cell adhesion" and "positive regulation of apoptotic process") were enriched in cluster 1 compared to clusters 2 and 8 (Fig. 5D). It is notable that cluster 1 resembles a previously described EndoMT cluster from the murine aorta [29], which may potentially act in concert with inflammation [23]. Overall, EC exposed to HSS in diseased arteries (*Apoe*$^{-/-}$ HFD) are enriched for transcriptional signatures associated with inflammation and apoptosis.

We next focused on mechanoreceptors because they are key regulators of the shear stress response acting upstream from inflammatory and apoptotic pathways. The expression of putative mechanoreceptors was compared in *Nos3*^{high} and *Nos3*^{low} cells in healthy arteries by analysis of the average levels of multiple mechanoreceptors

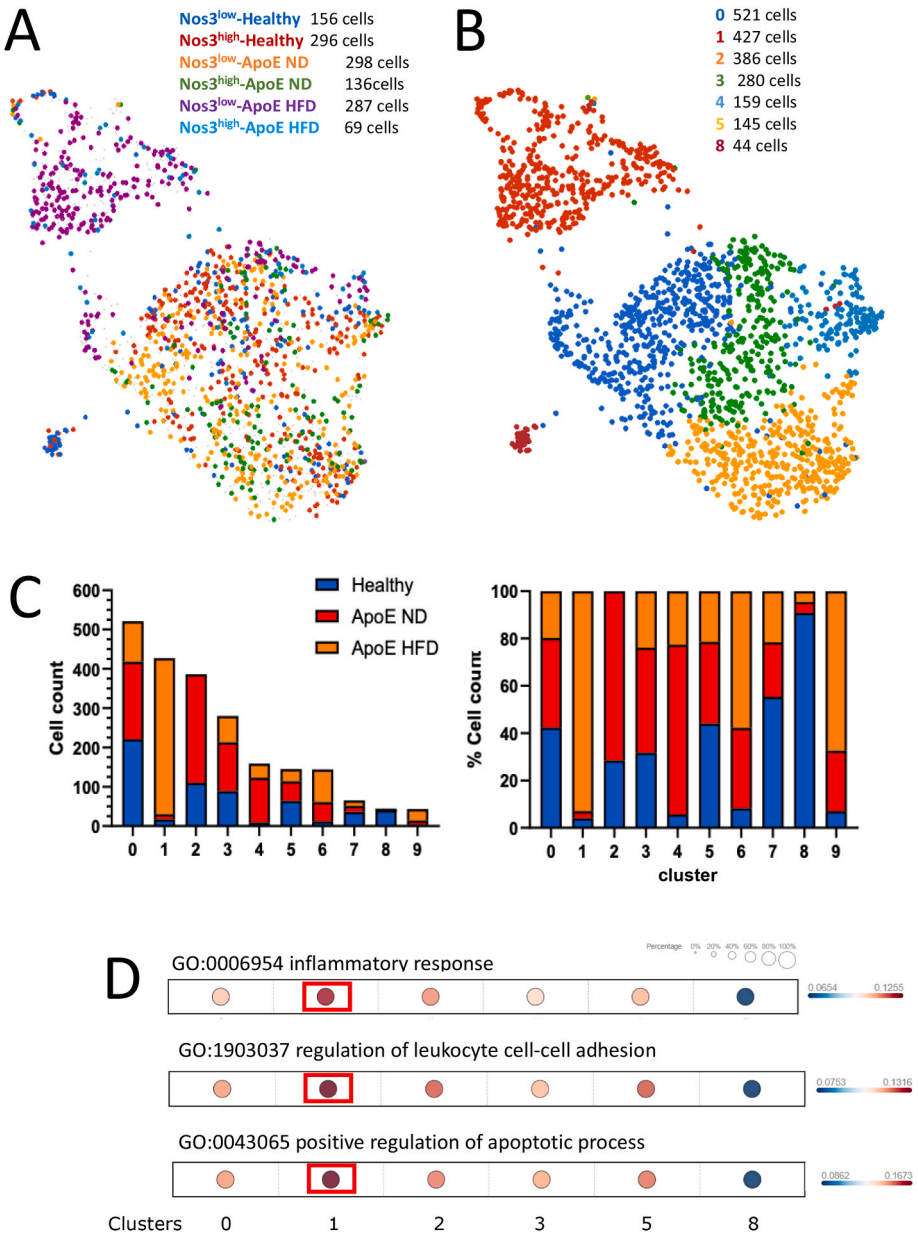

Fig. 5. scRNAseq reveals altered endothelial subsets in healthy and atherosclerotic murine aortas.
Aortas were isolated from healthy C57BL/6 mice, *ApoE*$^{-/-}$ mice exposed normal diet (ND) and *ApoE*$^{-/-}$ mice exposed to high fat diet (HFD) and were analysed by FACS of CD31^{+} CD45^{-} cells coupled to scRNAseq. Clusters were identified using unbiased hierarchical clustering. (A) UMAP showing the contribution of eNOS^{high} and eNOS^{low} cells from healthy, *ApoE*$^{-/-}$ ND and *ApoE*$^{-/-}$ HFD mice to each subpopulation. Non-endothelial clusters were excluded. (B) Clusters were identified using unbiased hierarchical clustering (as described in Supplementary Fig. S3). UMAP showing the cell contribution to canonical EC clusters and SMC. (C) eNOS^{high} cells were then selected and the frequency and proportion of cells from healthy, *ApoE*$^{-/-}$ ND and *ApoE*$^{-/-}$ HFD mice were quantified for each cluster. (D) Gene ontology terms associated with inflammation or apoptosis were quantified for canonical EC clusters and are presented as an intensity map of gene expression for specific EC clusters. Colour depicts the average level of expression of genes belonging to each GO term (varies between conditions); circle size depicts the proportion of cells that express genes belonging to each GO term (identical for each condition). (For interpretation of the references to colour in this figure legend, the reader is referred to the Web version of this article.)

(Supplementary Fig. S10) or by analysis of levels of individual mechanoreceptors (Supplementary Fig. S11; Supplementary Fig. S12). This revealed that mechanoreceptors were enriched in *Nos3*^{high} cells, which is consistent with a role in responses to physiological HSS. Intriguingly, the expression of mechanoreceptor genes in *Nos3*^{high} endothelium differed between healthy and diseased (*Apoe*$^{-/-}$ ND and *ApoE*$^{-/-}$ HFD) arteries (Supplementary Fig. S10; Supplementary Fig. S11; Supplementary Fig. S12), suggesting that mechanoresponses in EC under HSS may be altered in atherosclerotic plaques. However, the influence of atherosclerosis on the expression of putative mechanoreceptors is complex and varies between individual molecules. Some are increased in highly diseased arteries (*Apoe*$^{-/-}$ HFD) e.g. *Jcad, Sdc4, Heg1*, while others show the opposite pattern with a reduction in highly diseased arteries e.g. *Klk10, Notch1, Bmp4* (Supplementary Fig. S10B, Table S3). As a starting point to unravel this complexity, we focused on the atheroprotective mechanosensor *Klk10 which* was enriched in *Nos3*^{high} cells of healthy arteries but significantly reduced in *Nos3*^{high} cells of highly diseased arteries (*Apoe*$^{-/-}$ HFD; Supplementary Fig. S10B). This observation was confirmed at the protein level by *en face* immunofluorescent staining which showed that KLK10 was enriched at HSS regions of healthy and mildly diseased (*Apoe*$^{-/-}$ ND) aortas (Fig. 6 compare 1 vs. 2; compare 3 vs. 4). By contrast, KLK10 was absent from endothelium of highly diseased arteries (*Apoe*$^{-/-}$ HFD; Fig. 6 compare 2, 4 and 6). It was concluded that HSS-driven atheroprotection via KLK10 may be lost in conditions of highly atherosclerotic arteries compared to healthy arteries.

4. Discussion

The role of shear stress in atherosclerosis progression and the development of rupture-prone atherosclerotic plaques has been a subject of uncertainty and debate in the field [9,10]. Longitudinal studies assessing coronary arteries in patients with acute coronary syndrome have shown that physiological HSS predicts reduced plaque growth and fewer major adverse cardiac events [11–13]. However, physiological HSS has been associated with increased features of plaque instability in patients with stable angina [14]. While methodological differences and patient characteristics may contribute to these discrepancies [10], they also suggest that endothelial responses to shear stress may vary according to the disease state. To explore this concept, we conducted a comparative analysis of endothelial cells exposed to physiological HSS in healthy and diseased arteries.

The aortic arch serves as a valuable model for correlating shear stress with spatial variation in EC phenotypes, as *en face* immunofluorescence can be cross-referenced with shear stress maps using anatomical landmarks [30]. Analyzing the relationship between shear stress and EC features within atherosclerotic plaques poses challenges due to their complex geometry, which disrupts flow patterns. To overcome this obstacle, we developed a method that combines optical clearing, immunostaining, light sheet imaging, and computational fluid dynamics to analyze the spatial distribution of proteins and shear stress in atherosclerotic plaques. Using this approach, we demonstrated a spatial correlation between NOS3^{high} ECs and shear stress within atherosclerotic plaques. This method has broad applicability in correlating the expression of specific proteins with shear stress in vascular structures characterized by complex geometries.

The analysis of scRNAseq data presented here aligns with previous studies that have highlighted significant EC heterogeneity in both healthy and diseased arteries [22,27–29,31]. Andueza et al. [31] used scRNAseq and scATACseq to investigate the effects of flow on EC subsets in healthy mice subjected to carotid artery partial ligation. It was observed that the induction of disturbed flow (LSS) by partial ligation induced EC subsets that were enriched in pro-atherogenic genes including inflammatory, apoptotic and EndMT regulators, whereas steady flow (HSS) was associated with EC subsets enriched for protective factors [31]. Here we layer an additional level of complexity by assessing EC subsets in healthy and diseased arteries. By focusing on the *Nos3*^{high} subpopulation, we observed variations in the EC transcriptome under physiological HSS conditions between healthy and atherosclerotic arteries. Gene ontology analysis suggested that EC exposed to HSS were enriched for inflammatory and apoptotic transcripts in highly diseased

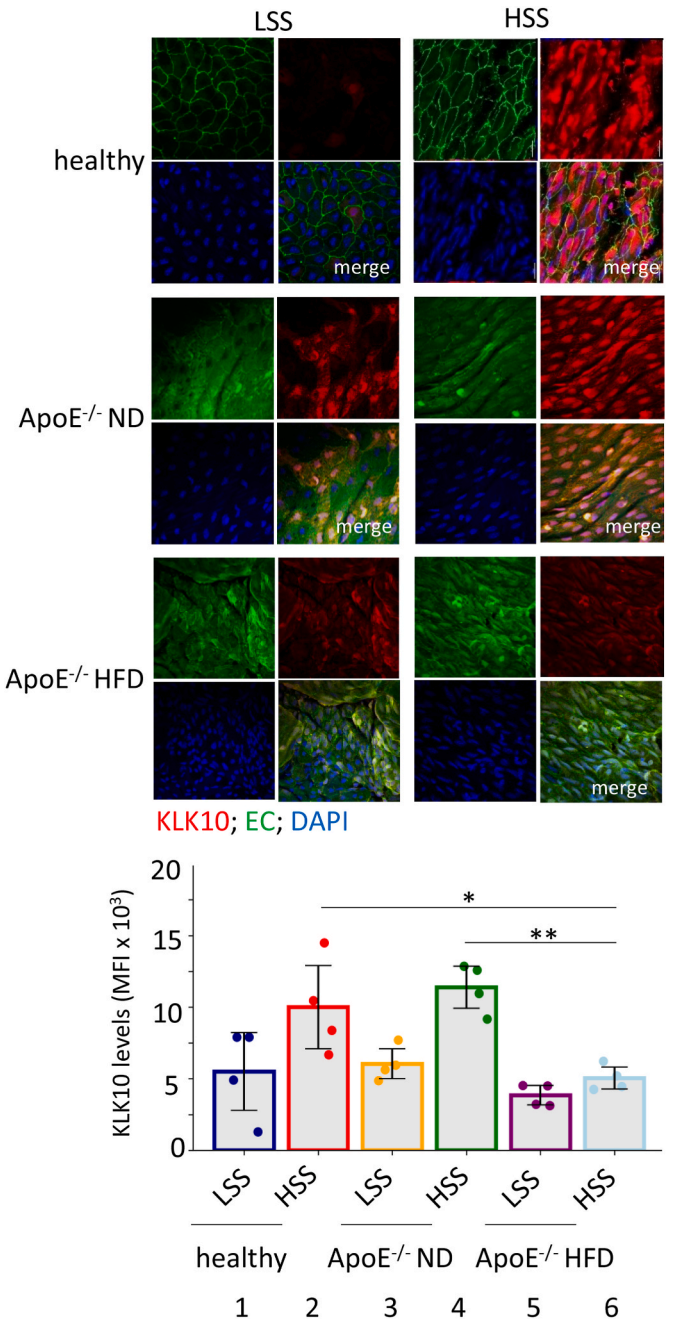

Fig. 6. KLK10 expression at regions of high shear stress is suppressed in atherosclerotic plaques.
Aortic arches were isolated from healthy C57BL/6 mice, *ApoE*$^{-/-}$ mice exposed normal diet (ND) and *ApoE*$^{-/-}$ mice exposed high fat diet (HFD). *En face* immunostaining was performed at regions of HSS (outer curvature) or LSS (inner curvature) using anti-KLK10 antibodies (red). Endothelial cells were co-stained (EC; CD31; green) and nuclei detected using DAPI (blue). Fluorescence was analysed by laser scanning confocal microscopy. Representative single fields of view are shown from outer and inner regions. Fluorescence was quantified at outer and inner portions; each data point represents an animal. Differences between means were analysed by two-way ANOVA. (For interpretation of the references to colour in this figure legend, the reader is referred to the Web version of this article.)

arteries, however further studies are needed to validate this. To unravel the molecular mechanisms underlying altered EC subsets in atherosclerosis, we focused on mechanosensors responsible for EC sensing of shear stress. Mechanosensors, including connexins, integrins, receptor tyrosine kinases, caveolae, adhesion molecules, and ion channels, convert shear stress into altered EC behaviour [1]. Through analysis of scRNAseq data, we demonstrated that putative mechanoreceptors exhibit divergent patterns of expression between healthy and atherosclerotic arteries. Some, like *Jcad, Sdc4,* and *Heg1*, are increased in HSS-EC of plaques, whereas others, such as *Klk10, Notch1*, and *BMP4*, show a reduction. These data suggest that mechanosensing may be altered in atherosclerotic arteries. However, given the diverse functions of mechanoreceptors the integration of multiple mechanosensory signals in the regulation of cell behaviour, it is challenging to predict the combined effects of these changes on EC physiology. To begin to interpret this complex system, we focused on a single established mechanoreceptor, KLK10, known for its role in atheroprotection [32]. This finding was corroborated at the protein level through *en face* staining of KLK10, a serine protease involved in shear stress sensing and known to protect against atherosclerosis by inhibiting inflammatory pathways [32]. KLK10 was prominently expressed in regions experiencing HSS in healthy aortas, yet it was notably diminished in ECs overlaying atherosclerotic plaques in *ApoE*$^{-/-}$ HFD mice. This reduction in KLK10 expression may contribute to the absence of vascular protection observed in regions of HSS within plaques. These observations are consistent with the study conducted by Williams et al. [32], which demonstrated a significant decrease in KLK10 expression levels in human coronary arteries with severe plaques compared to those with minimal plaques.

In summary, the transcriptome of ECs under physiological HSS displays variations between healthy and atherosclerotic arteries. Our scRNAseq analysis revealed that severe atherosclerosis leads to a loss of the anti-inflammatory shear stress sensor KLK10 at sites of HSS (Fig. 7). These findings provide a potential explanation for the observed correlation between physiological HSS and disease progression in certain clinical studies. The interplay between mechanosensors, altered EC subsets and shear stress underlines the complex relationship between blood flow and atherosclerosis, shedding light on the mechanisms driving disease pathogenesis and progression.

Financial support

This study was funded by a British Heart Foundation Programme Grant and a UKRI Future Leaders Fellowship.

Author contributions

ZZ, S-AK, JW, BT-A, EC, JW, MD, TS and MD made substantial contributions to the design of the study, and the acquisition, analysis and interpretation of data. MS, JW and MF made substantial contributions to the design of the study, and analysis and interpretation of data and reviewed the manuscript for important intellectual content. PCE made substantial contributions to the design of the study, analysis and interpretation of data, and drafted the manuscript. All authors gave their approval for the final version of the manuscript.

Declaration of competing interest

The authors declare the following financial interests/personal relationships which may be considered as potential competing interests:

Paul Evans reports financial support was provided by British Heart Foundation. Maria Fragiadaki reports financial support was provided by UK Research and Innovation. The other authors declare that they have no known competing financial interests or personal relationships that could have appeared to influence the work reported in this paper.

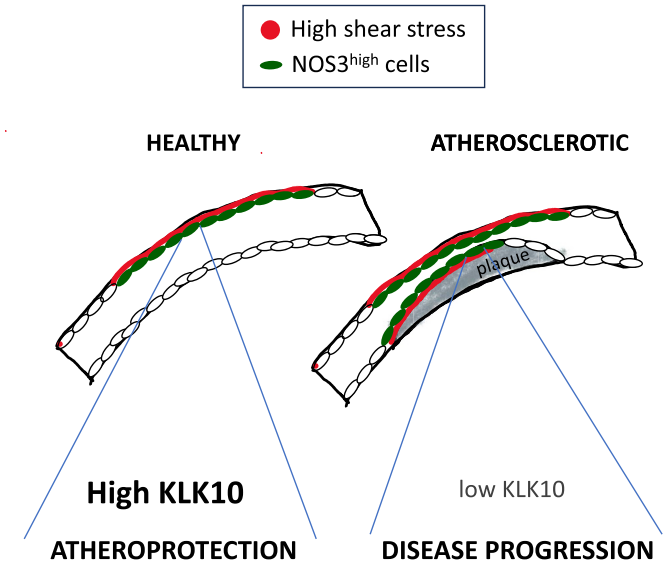

Fig. 7. Graphical abstract.
Light-sheet imaging coupled to computational fluid dynamics revealed that NOS3 is a marker of HSS in healthy arteries and atherosclerotic arteries. Using NOS3 as a marker, scRNAseq and *en face* staining revealed that the shear-sensitive atheroprotective factor KLK10 is lost from HSS endothelium in atherosclerosis. This uncoupling of KLK10 from HSS may explain in part the clinical observation of atherosclerosis progression at sites of HSS in some individuals.

Appendix A. Supplementary data

Supplementary data to this article can be found online at https://doi.org/10.1016/j.atherosclerosis.2024.118622.

References

[1] B.R. Kwak, M. Baeck, M.L. Bochaton-Piallat, G. Caligiuri, M.J. Daemens, P. F. Davies, I.E. Hoefer, P. Holvoet, H. Jo, R. Krams, S. Lehoux, C. Monaco, S. Steffens, R. Virmani, C. Weber, J.J. Wentzel, P.C. Evans, Biomechanical factors in atherosclerosis: mechanisms and clinical implications, Eur. Heart J. 35 (2014), 3013-+.
[2] A.J. Brown, Z. Teng, P.C. Evans, J.H. Gillard, H. Samady, M.R. Bennett, Role of biomechanical forces in the natural history of coronary atherosclerosis, Nat. Rev. Cardiol. 13 (2016) 210–220.
[3] P.F. Davies, Hemodynamic shear stress and the endothelium in cardiovascular pathophysiology, Nat. Clin. Pract. Cardiovasc. Med. 6 (2009) 16–26.
[4] I. Xanthis, C. Souilhol, J. Serbanovic-Canic, H. Roddie, A.C. Kalli, M. Fragiadaki, R. Wong, D.R. Shah, J.A. Askari, L. Canham, N. Akhtar, S. Feng, V. Ridger, J. Waltho, E. Pinteaux, M.J. Humphries, M.T. Bryan, P.C. Evans, Beta 1 integrin is a sensor of blood flow direction, J. Cell Sci. 132 (2019).
[5] C.G. Caro, J.M. Fitz-Gerald, R.C. Schroter, Arterial wall shear and distribution of early atheroma in man, Nature 223 (1969) 1159–1160.
[6] C. Cheng, D. Tempel, R. van Haperen, A. van der Baan, F. Grosveld, M.J. Daemen, R. Krams, R. de Crom, Atherosclerotic lesion size and vulnerability are determined by patterns of fluid shear stress, Circulation 113 (2006) 2744–2753.
[7] K.C. Koskinas, C.L. Feldman, Y.S. Chatzizisis, A.U. Coskun, M. Jonas, C. Maynard, A.B. Baker, M.I. Papafaklis, E.R. Edelman, P.H. Stone, Natural history of experimental coronary atherosclerosis and vascular remodeling in relation to endothelial shear stress, Circulation 121 (2010) 2092–2092U2042.
[8] A. Hoogendoorn, A.M. Kok, E.M.J. Hartman, G. de Nisco, L. Casadonte, C. Chiastra, A. Coenen, S.A. Korteland, K. Van der Heiden, F.J.H. Gijsen, D.J. Duncker, A.F. W. van der Steen, J.J. Wentzel, Multidirectional wall shear stress promotes advanced coronary plaque development: comparing five shear stress metrics, Cardiovasc. Res. 116 (2020) 1136–1146.
[9] P.C. Evans, M. Fragiadaki, P.D. Morris, J. Serbanovic-Canic, Shear stress: the dark energy of atherosclerotic plaques, Cardiovasc. Res. 117 (2021) 1811–1813.
[10] F. Gijsen, Y. Katagiri, P. Barlis, C. Bourantas, C. Collet, U. Coskun, J. Daemen, J. Dijkstra, E. Edelman, P. Evans, K. van der Heiden, R. Hose, B.-K. Koo, R. Krams, A. Marsden, F. Migliavacca, Y. Onuma, A. Ooi, E. Poon, H. Samady, P. Stone, K. Takahashi, D. Tang, V. Thondapu, E. Tenekecioglu, L. Timmins, R. Torii, J. Wentzel, P. Serruys, Expert recommendations on the assessment of wall shear stress in human coronary arteries: existing methodologies, technical considerations, and clinical applications, Eur. Heart J. 40 (2019) 3421–3433.
[11] P.H. Stone, A.U. Coskun, S. Kinlay, J.J. Popma, M. Sonka, A. Wahle, Y. Yeghiazarians, C. Maynard, R.E. Kuntz, C.L. Feldman, Regions of low endothelial

shear stress are the sites where coronary plaque progresses and vascular remodelling occurs in humans: an in vivo serial study, Eur. Heart J. 28 (2007) 705–710.
[12] P.H. Stone, S. Saito, S. Takahashi, Y. Makita, S. Nakamura, T. Kawasaki, A. Takahashi, T. Katsuki, S. Nakamura, A. Namiki, A. Hirohata, T. Matsumura, S. Yamazaki, H. Yokoi, S. Tanaka, S. Otsuji, F. Yoshimachi, J. Honye, D. Harwood, M. Reitman, A.U. Coskun, M.I. Papafaklis, C.L. Feldman, P. Investigators, Prediction of progression of coronary artery disease and clinical outcomes using vascular profiling of endothelial shear stress and arterial plaque characteristics the PREDICTION study, Circulation 126 (2012), 172-+.
[13] P.H. Stone, A. Maehara, A.U. Coskun, C.C. Maynard, M. Zaromytidou, G. Siasos, I. Andreou, D. Fotiadis, K. Stefanou, M. Papafaklis, L. Michalis, A.J. Lansky, G. S. Mintz, P.W. Serruys, C.L. Feldman, G.W. Stone, Role of low endothelial shear stress and plaque characteristics in the prediction of nonculprit major adverse cardiac events: the PROSPECT study, JACC Cardiovasc Imaging 11 (2018) 462–471.
[14] H. Samady, P. Eshtehardi, M.C. McDaniel, J. Suo, S.S. Dhawan, C. Maynard, L. H. Timmins, A.A. Quyyumi, D.P. Giddens, Coronary artery wall shear stress is associated with progression and transformation of atherosclerotic plaque and arterial remodeling in patients with coronary artery disease, Circulation 124 (2011) 779–788.
[15] C. Souilhol, J. Serbanovic-Canic, M. Fragiadaki, T.J. Chico, V. Ridger, H. Roddie, P. C. Evans, Endothelial responses to shear stress in atherosclerosis: a novel role for developmental genes, Nat. Rev. Cardiol. 17 (2020) 52–63.
[16] J.P. Green, C. Souilhol, I. Xanthis, L. Martinez-Campesino, N.P. Bowden, P. C. Evans, H.L. Wilson, Atheroprone flow activates inflammation via endothelial ATP-dependent P2X7-p38 signalling, Cardiovasc. Res. 114 (2018) 324–335.
[17] E.A. Susaki, K. Tainaka, D. Perrin, H. Yukinaga, A. Kuno, H.R. Ueda, Advanced CUBIC protocols for whole-brain and whole-body clearing and imaging, Nat. Protoc. 10 (2015) 1709–1727.
[18] N.S. Au - Kirkby, L. Au - Low, J. Au - Wu, E. Au - Miller, J.R. Au - Seckl, B.R. Au - Walker, D.J. Au - Webb, P.W.F. Au - Hadoke, Generation and 3-dimensional quantitation of arterial lesions in mice using optical projection tomography, JoVE (2015) e50627.
[19] A. Fedorov, R. Beichel, J. Kalpathy-Cramer, J. Finet, J.C. Fillion-Robin, S. Pujol, C. Bauer, D. Jennings, F. Fennessy, M. Sonka, J. Buatti, S. Aylward, J.V. Miller, S. Pieper, R. Kikinis, 3D slicer as an image computing platform for the quantitative imaging network, Magn. Reson. Imaging 30 (2012) 1323–1341.
[20] L. Antiga, M. Piccinelli, L. Botti, B. Ene-Iordache, A. Remuzzi, D.A. Steinman, An image-based modeling framework for patient-specific computational hemodynamics, Med. Biol. Eng. Comput. 46 (2008) 1097–1112.
[21] L. Luong, H. Duckles, T. Schenkel, M. Mahmoud, J.L. Tremoleda, M. Wylezinska-Arridge, M. Ali, N.P. Bowden, M.C. Villa-Uriol, K. van der Heiden, R. Xing, F. J. Gijsen, J. Wentzel, A. Lawrie, S. Feng, N. Arnold, W. Gsell, A. Lungu, R. Hose, T. Spencer, I. Halliday, V. Ridger, P.C. Evans, Heart rate reduction with ivabradine promotes shear stress-dependent anti-inflammatory mechanisms in arteries, Thromb. Haemostasis 116 (2016) 181–190.
[22] C. Souilhol, B.T. Ayllon, X.Y. Li, M.R. Diagbouga, Z.Q. Zhou, L. Canham, H. Roddie, D. Pirri, E.V. Chambers, M.J. Dunning, M. Ariaans, J. Li, Y. Fang, H.F. Jorgensen, M. Simons, R. Krams, J. Waltenberger, M. Fragiadaki, V. Ridger, S. De Val, S. E. Francis, T.J.A. Chico, J. Serbanovic-Canic, P.C. Evans, JAG1-NOTCH4 mechanosensing drives atherosclerosis, Sci. Adv. 8 (2022).
[23] P.Y. Chen, L. Qin, G. Li, Z. Wang, J.E. Dahlman, J. Malagon-Lopez, S. Gujja, N. A. Cilfone, K.J. Kauffman, L. Sun, H. Sun, X. Zhang, B. Aryal, A. Canfran-Duque, R. Liu, P. Kusters, A. Sehgal, Y. Jiao, D.G. Anderson, J. Gulcher, C. Fernandez-Hernando, E. Lutgens, M.A. Schwartz, J.S. Pober, T.W. Chittenden, G. Tellides, M. Simons, Endothelial TGF-β signalling drives vascular inflammation and atherosclerosis, Nat. Metab. 1 (2019) 912–926.
[24] V. Garcia, W.C. Sessa, Endothelial NOS: perspective and recent developments, Br. J. Pharmacol. 176 (2019) 189–196.
[25] D. Won, S.N. Zhu, M. Chen, A.M. Teichert, J.E. Fish, C.C. Matouk, M. Bonert, M. Ojha, P.A. Marsden, M.I. Cybulsky, Relative reduction of endothelial nitric-oxide synthase expression and transcription in atherosclerosis-prone regions of the mouse aorta and in an in vitro model of disturbed flow, Am. J. Pathol. 171 (2007) 1691–1704.
[26] J. Suo, D.E. Ferrara, D. Sorescu, R.E. Guldberg, W.R. Taylor, D.P. Giddens, Hemodynamic shear stresses in mouse aortas: implications for atherogenesis, Arterioscler. Thromb. Vasc. Biol. 27 (2007) 346–351.
[27] A.S. Kalluri, S.K. Vellarikkal, E.R. Edelman, L. Nguyen, A. Subramanian, P. T. Ellinor, A. Regev, S. Kathiresan, R.M. Gupta, Single-cell analysis of the normal mouse aorta reveals functionally distinct endothelial cell populations, Circulation 140 (2019) 147–163.
[28] E. Engelbrecht, M.V. Levesque, L. He, M. Vanlandewijck, A. Nitzsche, H. Niazi, A. Kuo, S.A. Singh, M. Aikawa, K. Holton, R.L. Proia, M. Kono, W.T. Pu, E. Camerer, C. Betsholtz, T. Hla, Sphingosine 1-phosphate-regulated transcriptomes in heterogenous arterial and lymphatic endothelium of the aorta, Elife 9 (2020).
[29] M.P.J. de Winther, M. Bäck, P. Evans, D. Gomez, I. Goncalves, H.F. Jørgensen, R. R. Koenen, E. Lutgens, G.D. Norata, E. Osto, L. Dib, M. Simons, K. Stellos, S. Ylä-Herttuala, H. Winkels, M.L. Bochaton-Piallat, C. Monaco, Translational opportunities of single-cell biology in atherosclerosis, Eur. Heart J. 44 (2023) 1216–1230.
[30] J. Serbanovic-Canic, A. de Luca, C. Warboys, P.F. Ferreira, L.A. Luong, S. Hsiao, I. Gauci, M. Mahmoud, S. Feng, C. Souilhol, N. Bowden, J.P. Ashton, H. Walczak, D. Firmin, R. Krams, J.C. Mason, D.O. Haskard, S. Sherwin, V. Ridger, T.J. Chico, P. C. Evans, Zebrafish model for functional screening of flow-responsive genes, Arterioscler. Thromb. Vasc. Biol. 37 (2017) 130–143.
[31] A. Andueza, S. Kumar, J. Kim, D.W. Kang, H.L. Mumme, J.I. Perez, N. Villa-Roel, H. Jo, Endothelial reprogramming by disturbed flow revealed by single-cell RNA and chromatin accessibility study, Cell Rep. 33 (2020) 108491.
[32] D. Williams, M. Mahmoud, R. Liu, A. Andueza, S. Kumar, D.W. Kang, J. Zhang, I. Tamargo, N. Villa-Roel, K.I. Baek, H. Lee, Y. An, L. Zhang, E.W. Tate, P. Bagchi, J. Pohl, L.O. Mosnier, E.P. Diamandis, K. Mihara, M.D. Hollenberg, Z. Dai, H. Jo, Stable flow-induced expression of KLK10 inhibits endothelial inflammation and atherosclerosis, Elife 11 (2022).